JACS
JOURNAL OF THE AMERICAN CHEMICAL SOCIETY
pubs.acs.org/JACS
Article

Real-Time Multiscale Imaging of Heterogeneous Multistage Reactions: Insights into Nanoscale TiO_2 Synthesis

Bryan A. Sanchez Monserrate, Michelle L. Beauvais, Simon M. Vornholt, Peter J. Chupas, John B. Parise, and Karena W. Chapman*

Cite This: J. Am. Chem. Soc. 2024, 146, 10745−10752
Read Online
ACCESS | Metrics & More | Article Recommendations | Supporting Information

ABSTRACT: Hydrothermal methods are widely used to synthesize functional inorganic materials. The interplay between the reactive species, solution chemistry, and the nanoscale product makes it challenging to control the reaction pathway to achieve a uniform product. Here, we resolve the heterogeneity that arises during hydrothermal synthesis across different length scales. We combine spatially resolved *in situ* X-ray pair distribution function (PDF) and small-angle X-ray scattering analysis, which are sensitive to structure on the atomic and nanoscale, with a novel time-lapse optical imaging strategy that reveals heterogeneity and phase separations across the entire reaction. For TiO_2 synthesis *via* hydrothermal hydrolysis of $TiCl_4$, we identify multiple cycles of TiO_2 formation and separation that contribute to nonuniformity in the polymorphic product. The PDF data show that the characteristics of TiO_2 formed during each formation−separation cycle differ, contributing to the ongoing challenge of precisely identifying reaction controls. The imaging strategy pioneered here provides an efficient *in situ* means to systematically compare how the reaction evolves under different chemical conditions, thereby advancing our understanding of functional inorganic material synthesis.

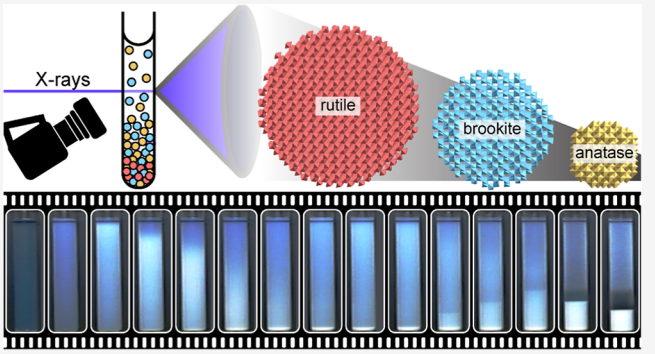

INTRODUCTION

Understanding and manipulating how nanomaterials evolve during synthesis are critical to deliberately controlling their physicochemical properties. However, due to the complex interdependence of the synthesis chemistry and the nanoparticle characteristics, it is challenging to identify how individual reaction parameters affect the phase evolution, morphology, surface structure and chemistry, and the distribution of defects within the eventual product.[1,2] In solution-phase synthesis, which allows precise control over nanoparticle size, shape, and composition using molecular precursors and structure-directing agents,[3] the nature of the nanoparticle product depends on the interface with the solution environment; in turn, the solution environment evolves as precursors react to form nanoparticles.

Solution-phase syntheses are typically evaluated using a "cook-and-look" approach, iteratively testing the product resulting from different sets of reaction conditions.[4] In the case of nanoscale TiO_2, which is widely explored for photoenergy conversion applications,[5−7] thousands of studies have evaluated different synthesis conditions (e.g., temperature, Ti precursor, concentration, pH, and additives) and the characteristics and functionality of the resulting TiO_2.[4,8−10] Defect-rich TiO_2 nanoparticles with lower-energy band gaps are desirable because they allow more-efficient photocatalysis and solar energy conversion.[7,11,12] Despite the preponderance of synthetic studies of this material, these primarily report the outcome of a given set of reaction parameters. A fundamental mechanistic understanding of how the choice of synthesis reaction parameters influences the reaction pathway remains elusive.

In typical TiO_2 syntheses *via* hydrothermal hydrolysis, the product is a mixture of polymorphs,[13] including rutile, the thermodynamically stable bulk phase, as well as anatase and brookite, which are stabilized for small particles (<11 nm and 11−35 nm, respectively).[14−16] During the reaction, precursors such as $TiCl_4$ undergo hydrolysis and then condense to form insoluble TiO_2. This mechanism is intrinsically heterogeneous involving dynamic, coupled changes to the solution speciation, surface energy, nucleation and growth, and eventual separation of the solid product.[17−19] This complex interdependent heterogeneity not only presents a challenge when targeting specific physicochemical properties, but it also makes it more

Received: January 16, 2024
Revised: March 25, 2024
Accepted: March 26, 2024
Published: April 8, 2024

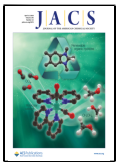

https://doi.org/10.1021/jacs.4c00749
J. Am. Chem. Soc. 2024, 146, 10745−10752

difficult to target a phase-pure, uniform product.[20,21] Compared to evaluating the reaction outcome *post facto*, monitoring the reaction progress continuously in real time has the potential to uncover fundamental mechanistic understanding of the reaction pathway.

Here, we combine *in situ* approaches to probe the heterogeneity that arises across multiple scales during the TiO_2 synthesis. While X-ray diffraction tools are a gold standard for such *in situ* studies,[22−26] we combine X-ray approaches with rapid, real-time optical imaging, in a new methodology that can be readily extended to other systems. Specifically, we combine conventional *in situ* X-ray scattering tools, including small-angle X-ray scattering (SAXS) and pair distribution function (PDF) analyses, which are sensitive to structure on the atomic and nanoscale,[23,24,27] with quantitative analysis of *in situ* optical imaging to visualize the spatiotemporal heterogeneity that emerges within the reacting system.

These analyses reveal multiple discrete cycles of TiO_2 formation and separation with different polymorph distributions and particle sizes accumulating during each cycle. The recognition of this emergent heterogeneity, and discrete cycles of formation and sedimentation, is critical for understanding batch-scale nanomaterial synthesis and how the nanomaterial product depends on the evolving reaction conditions. Importantly, the optical imaging analysis, based on the *RGB* pixel values, is demonstrated to be a valuable and accessible tool to derive quantitative information on such reactions, systematically evaluating many variations of the reaction in parallel, to quantify the kinetics of product formation and separation, the hydrodynamic particle size, and how these depend on various reaction parameters.

EXPERIMENTAL METHODS

Time-Lapse Imaging. A series of time-lapse images were recorded during the formation of TiO_2 *via* hydrolysis of aqueous $TiCl_4$ in reactor tubes in the oven. The reagent solutions (0.5 mL) were sealed within tall 3 mm diameter glass tubes (14 cm tall tube and 7 cm tall solution) and heated at 95 °C in a custom 3D-printed reaction holder within a convection oven for up to 30 days, while time-lapse optical images were acquired at 10 s intervals using a 1080p webcam (Logitech C920x). The images were color-corrected, and the luminance values (Y) in regions of interest within the reaction image were calculated from the red (R), green (G), and blue (B) pixel values based on the relationship $Y = R(0.2126) + G(0.7152) + B(0.0722)$, which reflects the sensitivity of human vision.

X-ray Scattering Measurements. Spatially resolved *in situ* X-ray scattering data suitable for SAXS and PDF analysis were collected during the formation of TiO_2 *via* hydrolysis of aqueous $TiCl_4$. The reagent solution (0.08 mL) was sealed within short 3 mm diameter glass tubes (2.7 cm tall tube and 1.2 cm tall solution) and heated at 95 °C using an X-ray compatible reactor.[28] The reaction mixture was probed at different heights. For SAXS measurements at beamline 11-BM of the National Synchrotron Light Source-II at Brookhaven National Laboratory, the beam probed two static positions: just below the solution surface and the bottom of the reaction. For X-ray PDF experiments at beamline 11-ID-B of the Advanced Photon Source at Argonne National Laboratory, the beam probed positions just below the solution surface and a raster of the bottom 25% of the reaction. Some timing variability is evident between measurements due to the different heating environments and rates; however, the relative trends (e.g., for the various concentrations) remain consistent.

RESULTS

Time-Lapse Imaging and Luminance Analysis. A series of time-lapse images, recorded during the hydrolysis reaction in tall reactor tubes in an oven, reveal a spatial heterogeneity that develops in the reaction (Figure 1).

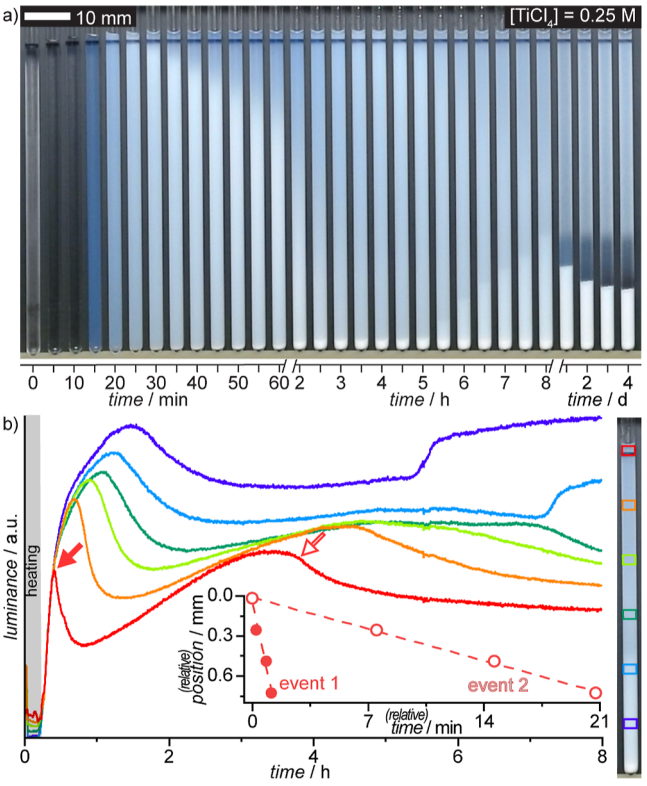

Figure 1. (a) Time-lapse images obtained during the synthesis of nanoscale TiO_2, *via* hydrolysis of $TiCl_4$ (0.25 M), show two distinct cycles of product formation and separation. (b) Time dependence of the luminance values at various heights within the reactor is different, reflecting the spatial heterogeneity. The trends immediately beneath the solution surface most directly reflect the kinetics of formation sedimentation (inset). The maxima in the luminance at different heights can be used to evaluate the sedimentation velocities.

The luminance values within the color-corrected images evolve during the reaction, which we propose serves as a photometric measure of the solution turbidity. This reflects the TiO_2 product concentration, increasing as TiO_2 particles form, then decreasing as the TiO_2 colloid destabilizes and sediments to the bottom of the reactor.[29,30] Thus, the images allow us to quantify the kinetics of TiO_2 formation and separation, resolving heterogeneity in the TiO_2 distribution as a continuous function of height within the reactor and how these depend on reagent concentration.

In the first 20 min, the solution height increases owing to thermal expansion. Once at temperature, the solution turns uniform blueish and then bright white as colloidal TiO_2 forms (Figure 1a). Subsequently, there is a decrease in turbidity that propagates downward from the top of the solution, as the TiO_2 colloid destabilizes. The turbidity at intermediate heights within the reactor temporarily increases as the TiO_2 product sediments to the bottom of the reactor. The turbidity then increases uniformly again before a second sedimentation event.

The spatially heterogeneous distribution of the product within the solution is seen in the different evolution of the

https://doi.org/10.1021/jacs.4c00749
J. Am. Chem. Soc. 2024, 146, 10745−10752

luminance within regions of interest at different heights within the reaction tube (Figure 1b). Consider, for example, the first formation and sedimentation event. Near the top of the solution, the luminance reaches a maximum value at ~25 min, after which the solid product starts to sink. Deeper within the solution, the luminance continues to increase as product falls from above and only reaches a maximum after ~90 min as the solid sedimentation front passes this point. The redistribution of the product during the reaction means that different trends in the product distribution are evident at different heights.

The time points at which the luminance attains a maximum value at different heights can be used to estimate the velocity of product sedimentation (Figure 1b, inset). The different rates at which the solids sink reflect the difference in the product accumulated in each cycle, with much slower sedimentation for the second cycle compared to the first (0.034 *cf* 0.29 mm·min^{-1}). For particles with similar densities and morphologies, larger particles sink faster than smaller particles.[31] This suggests that in the present reactions, larger particles are accumulated during the first compared to the second sedimentation event and at higher compared to lower concentrations. In addition to the average, the uniformity of particle sizes can also be determined. Products with a narrow size distribution will sediment at the same rate, producing a sharp, well-defined sedimentation front, while products with a broad size distribution will sediment at different rates, producing a diffuse, broadened sedimentation front. Because of the potential for the separation of particles of different sizes as they sink, the sedimentation velocity near the top of the solution provides the most reliable estimate of the average sedimentation velocity.

The pixel luminance just beneath the solution surface directly reflects the time-dependent changes in the TiO_2 concentration and how these vary for the reaction of different $TiCl_4$ concentrations (Figure 2). The onset time for

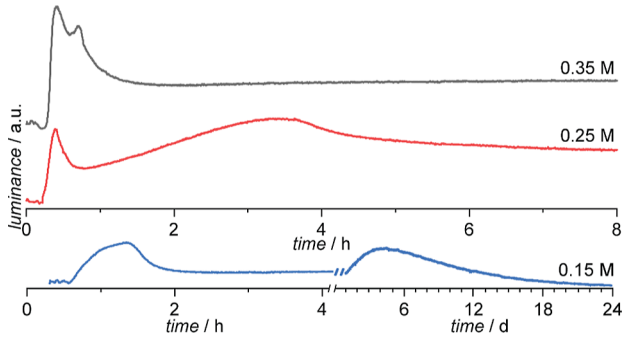

Figure 2. Subsurface luminance, which directly reflects kinetics of TiO_2 formation and sedimentation, shows two sedimentation events for all concentrations, with slower time scales for lower concentrations.

sedimentation, the velocity of sedimentation, and the amount of solid accumulated obtained for these reactions from the time-lapse imaging and luminance analysis are summarized in Table 1.

These subsurface luminance values allow quantitative comparison of the two distinct sedimentation events for all reaction concentrations studied and show that these are delayed to longer reaction times for lower $TiCl_4$ concentrations. Continued imaging over 30 days shows that no further product forms after the second sedimentation event,

Table 1. TiO_2 Sedimentation Events from Time-Lapse Imaging

$[TiCl_4]$	event	time	accumulated solid/mm	velocity mm·min^{-1}
0.35 M	1	25 min	1	4.9 (7) × 10^{-1}
	2	43 min	18	[a]
0.25 M	1	23 min	1	2.9 (5) × 10^{-1}
	2	3 h 40 min	27	3.39 (11) × 10^{-2}
0.15 M	1	1 h	1	8.88 (14) × 10^{-2}
	2	5.5 d	20	1.52 (8) × 10^{-3}

[a]Overlaps with the first sedimentation front.

although the accumulated solid continues to compact (see the Supporting Information).

Spatially Resolved *In Situ* SAXS Analysis. The *in situ* SAXS data confirm the two cycles of particle formation and sedimentation. The SAXS data are sensitive to particle size distribution and can be used to quantify how this evolves during the reaction and to evaluate the size of the particles that settle during each sedimentation event.

The SAXS data were modeled using a distribution of spherical particles with a multimodal distribution (Figure 3). A

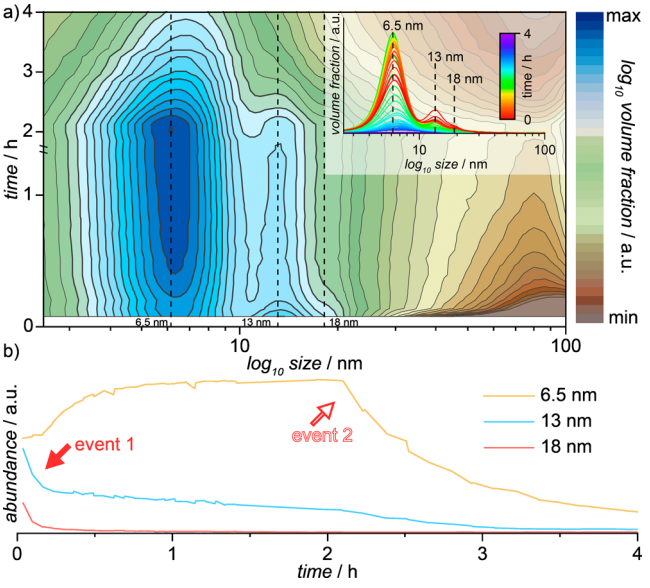

Figure 3. (a) Time-resolved size distribution from *in situ* SAXS analysis (subsurface) of 0.25 M $TiCl_4$, and (b) the corresponding abundance of the characteristic particle size populations.

bimodal distribution of spherical particles can suggest rod- or plate-like particles; here, a spherical particle morphology is supported by transmission electron microscopy imaging of the recovered product (Supporting Information) from the top layer (i.e., from the second sedimentation event). However, some larger nanorod agglomerates, a common morphology associated with rutile, were found in the bottom layer.

During the reaction, the populations of particles with different characteristic sizes change, without significant change in the characteristic sizes themselves (Figure 3a). During the initial TiO_2 formation, 3−4 distinct particle sizes are evident near the solution surface, with populations centered at ~6.5, 13, and 18 nm and a minor population of larger particles for a reaction of 0.25 M $TiCl_4$. For the reaction of a lower concentration, 0.15 M $TiCl_4$, a similar particle size distribution

https://doi.org/10.1021/jacs.4c00749
J. Am. Chem. Soc. 2024, 146, 10745−10752

is observed. For a reaction of higher concentration, 0.35 M $TiCl_4$, the particle size distribution is again similar but with slightly larger particles with populations centered at ∼6.6, 14, 20, and 25 nm. For all concentrations, the particles with the smallest size, ∼6.5 nm, represent the largest volume fraction, followed by the intermediate-sized particles and the largest particles.

During the first sedimentation event, the population of the large- and intermediate-sized particles decreases (and disappears for the largest particles, ≥18 nm) as these sink below the path of the X-ray beam (Figure 3b). Following the first sedimentation, the population of the smallest particles increases up to a second sedimentation, where the population of all particles drops as they sink below the path of the X-ray beam. This is most clearly visualized for the reaction of 0.25 M $TiCl_4$. The rate of particle formation and the subsequent sedimentation are faster for higher concentrations. For a reaction at higher concentration with 0.35 M $TiCl_4$, the two sedimentation events are more closely spaced so that the distinction between the two events is less clear. For a reaction at lower concentration with 0.15 M $TiCl_4$, only the initial growth is observed; the two sedimentation events were not observed within the time limit of the synchrotron experiment. Near the bottom of the reactor, commensurate trends reflect accumulation of the solid product within the volume probed by the X-ray beam (see the Supporting Information).

Based on the change in abundance of different particle populations during each sedimentation event, the average size of the particles that sink during each sedimentation event was estimated (see the Supporting Information). This analysis demonstrates that for each reaction concentration, particles that sink during the first sedimentation event are on average larger than those that sink during the second event. Similarly, for the reaction at higher concentration, the particles that sink during each sedimentation event are on average larger than those for the reaction at lower concentration.

Spatially Resolved *In Situ* X-Ray PDF Analysis. The two reactor positions probed by the X-ray beam show different trends in the amount of TiO_2 product that reflect the settling of the solid to the bottom of the reactor. Near the solution surface, the data show that TiO_2 forms immediately, with two abrupt drops in signal at 1.5 and 3.4 h, after which little TiO_2 remains suspended. Near the bottom of the reactor, the data show a signal from TiO_2 throughout the reaction: TiO_2 forms immediately, with an abrupt increase in the signal at ∼1.5 h and a further change at 3.4 h.

To evaluate the atomic and nanoscale structure of the TiO_2 product formed during the reaction, structure models were refined against the *in situ* PDF data within PDFgui.[32] This analysis identified mixtures of nanoscale anatase and brookite and bulk rutile as the polymorphic products of the reaction (Figure 4).

Anatase is the dominant product with a smaller proportion of brookite and a minor component of rutile. Initially, similar proportions of nanoscale brookite and anatase form, then anatase increases, and a minor rutile component forms. When TiO_2 sediments, the amounts of rutile and brookite in solution drop more than anatase. Rutile only forms during the first formation−sedimentation cycle, while the second formation−sedimentation cycle is richer in anatase than in brookite. At the bottom of the reactor (see the Supporting Information), the phase distribution up to the first sedimentation mirrors the trends evident near the top of solution. Following the first

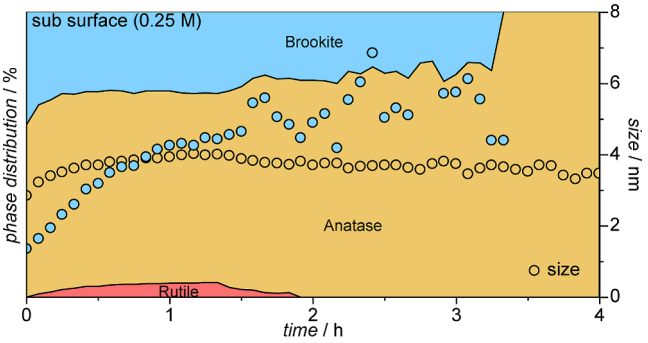

Figure 4. Polymorphic phase distribution and coherent particle size from the analysis of *in situ* PDF data measured just under the solution surface for the reaction of 0.25 M $TiCl_4$.

sedimentation, there is an increase in rutile and a smaller relative increase in anatase and brookite, as the solid collects from above.

For the reaction of higher-concentration 0.35 M $TiCl_4$, the phase distribution shows trends similar to those of the 0.25 M reaction but with faster kinetics and with slightly higher proportions of anatase and rutile (see the Supporting Information). For the reaction of lower-concentration 0.15 M $TiCl_4$, there is less rutile, and the two sedimentation events were not observed within the time limit of the synchrotron experiment.

The coherent domain size for the anatase particles in solution varies from 3 to 4 nm up to the first sedimentation, drops slightly, then stabilizes. The coherent domain size for brookite increases from 2 to ∼6 nm. The domain size for rutile was larger than can be effectively quantified based on the PDF data (∼10 nm), and so this was refined as a bulk phase.

While both PDF and SAXS data are sensitive to particle size, the sizes of the coherent structural domains refined for brookite and anatase based on the PDF data are smaller than the characteristic particle populations seen in the *in situ* SAXS data (Figure 3). It is reasonable to expect that for the same particles, the domain size refined based on PDF data will be equal to or lower than the particle size quantified through SAXS analysis. This is because the PDF evaluates the size of the coherent crystalline domain, which may be smaller than the physical particle. Several phenomena can contribute to the smaller size apparent in the PDF analysis: the structure at the particle surface may relax; the particles may incorporate substantial disorder such that the length scale over which the structure is well ordered is much smaller than the whole particle; or the particles may exist as polycrystalline aggregates (e.g., formed through particle attachment).[33,34] Indeed an increase in the length scale over which the atomic structure is ordered (i.e., crystallinity) within the brookite phase likely underlies variability in the refined domain size (2−6 nm) from the PDF, despite the average size of discrete particle populations remaining constant in the SAXS analysis.

Correlating Particle Size and Sedimentation Rate. We explore the relationship between the sedimentation velocity evaluated from the time-lapse imaging and the average physical particle size quantified from the SAXS analysis (Figure 5). For particles of similar density and morphology, the sedimentation velocity is correlated with the hydrodynamic size of the particles, with large particles sinking faster than small particles. For micron-scale particles, the particle size is related to the sedimentation velocity *via* Stokes law[35] which takes into

https://doi.org/10.1021/jacs.4c00749
J. Am. Chem. Soc. 2024, 146, 10745−10752

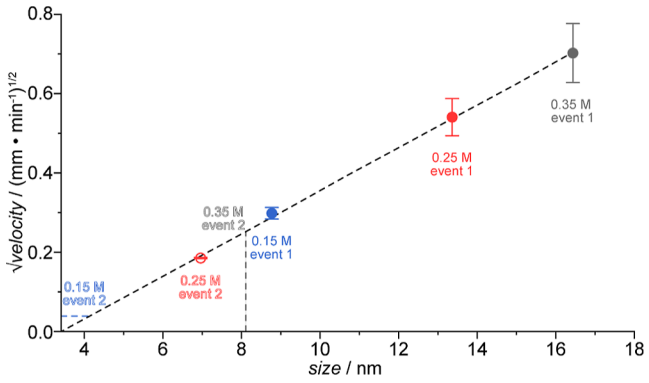

Figure 5. Average particle size at the onset of sedimentation determined from *in situ* SAXS measurements is linearly related to the √velocity (sedimentation) from imaging analysis, in a Stokes-like relationship. This relation can be used to estimate the size of particles in variants of this reaction.

account particle density, solution density, and solution viscosity. However, this relationship is known to break down for small nanoparticles.[36,37] Here, we see a Stokes-like linear relationship between the average size of the sedimenting particles from SAXS and the square root of the sedimentation velocity from the imaging analysis.

The linear relationship between size and √velocity (sedimentation) can be used to evaluate or compare the particle size in variants of this reaction based on the time-lapse imaging, potentially reducing or circumventing the need for synchrotron measurements. Similarly, it can be used to estimate the particle size for sedimentation events that occur at longer reaction times than can be accommodated within a synchrotron beamtime allocation. This includes the second sedimentation event for the lowest-concentration 0.15 M $TiCl_4$ reaction which occurs at much longer reaction time (~5 days) than the duration of either the SAXS or the PDF experiments. Based on the relationship between the sedimentation velocity and particle size observed here, the velocity seen for the second sedimentation of the 0.15 M, a ~4 nm average particle size is suggested.

DISCUSSION

The present time-lapse imaging analysis and spatially resolved *in situ* X-ray scattering study reveal a multistage mechanism for the synthesis of nanoscale TiO_2 *via* hydrolysis. Striking spatial heterogeneities appear and evolve as initially colloidal TiO_2 destabilizes and the solid sinks to the bottom of the reactor. Specifically, we resolve two such cycles of nanoparticle formation and growth, followed by destabilization, sedimentation, and separation of the solid product. The accumulated product at the bottom of the reactor does not change, no longer actively participating in the reaction. The characteristics of the TiO_2 formed in each cycle are different, which contributes to the nonuniformity of the product.

This spatiotemporal heterogeneity is a newly identified complexity in nanomaterial synthesis, for which predictive mechanistic understanding and polymorph control are already challenging. The destabilization of the TiO_2 colloid that leads to the observed sedimentation events and the different polymorph distribution produced during each cycle underscores the different reaction conditions and solution composition that exist as the reaction evolves.

During the reaction, the precursors undergo hydrolysis and then condense to form insoluble TiO_2 which is accompanied by a decrease in pH and an increase in the Cl^- concentration. We propose that evolving solution composition contributes to both the multicycle formation−destabilization−sedimentation behavior and the difference in the polymorph distribution within each stage of the reaction.

The sedimentation reflects destabilization of the TiO_2 colloid, that is, the electrostatic barrier that prevents particle aggregation in the initial colloid collapses. This can result from changes in the pH and/or ion concentrations in the solution that impact the surface charge. A consideration of how the composition of the solution evolves during the reaction (Figure 6, $TiCl_4 + H_2O \rightarrow TiO(H)_xCl_{4-x} + xCl^- + 2xH^+ \rightarrow$

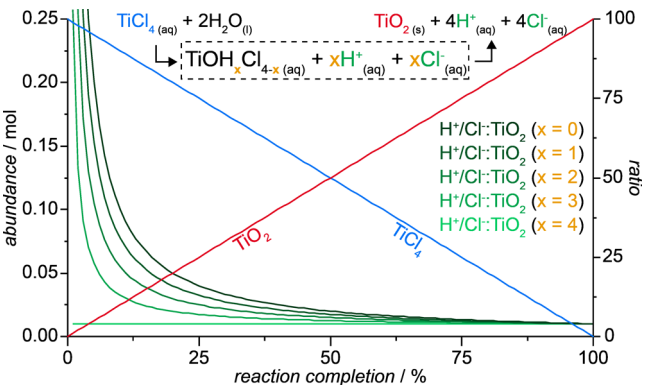

Figure 6. Illustration of how the solution composition could change as the hydrolysis reaction progresses.

$TiO_2 + 4Cl^- + 4H^+$) shows that early in the reaction (where the first sedimentation event is observed), the ratio of Cl^-/H^+ to TiO_2 product changes rapidly. This rapid change in the ion to nanoparticle product ratio (without significant particle growth) could contribute to the destabilization of the colloid and the sedimentation event. An implication of this hypothesis is that changing the ionic composition of the solution would moderate the sedimentation events.

The solution environment during the initial product formation and following the first sedimentation are different, which contributes to the different TiO_2 polymorph distribution. Notably, for nanoparticle phases, the surface energy has a significant, evolving contribution to the nanoparticle stability. As the reaction proceeds, the surface energy and chemistry change with changing solution species, concentration, and surface interactions. Furthermore, the surface-area-to-volume ratio, and hence, relative importance of the surface energy, also changes. The characteristics of the eventual nanomaterials produced are an integrated outcome of the evolving conditions and energetics through the reaction. In conventional batch synthesis or *ex situ* studies, the products formed in each cycle are not distinguished; importantly, the recovered product is the average of both precipitation events and thus does not reflect the product distribution produced at any individual stage during the reaction. The phase distribution in the final product will depend on when the reaction is halted. This likely contributes to the variability evident in TiO_2 synthesis studies.[4,8]

Although the size from the SAXS analysis is a more reliable measure of the physical particle size and surface area than the size from the PDF analysis, in SAXS, the particle size

https://doi.org/10.1021/jacs.4c00749
J. Am. Chem. Soc. 2024, 146, 10745−10752

information is not linked to a specific phase or polymorph. By contrast, for PDF analysis, the refined domain size is specific to each polymorph. Here, the smallest domains are seen for anatase, intermediate domains for brookite, and the largest bulk domains for the rutile phase. Matching this sequence of domain sizes, along with their relative abundance, through the particle formation and sedimentation, to the discrete particle populations from SAXS suggests that the ∼6.5 nm particles correspond to anatase, the 13−14 nm particles correspond to brookite, and the >18−20 nm particles correspond to rutile. The largest particles are only seen in SAXS during the initial particle formation and then sediment, as do the largest, bulk particles in the PDF which have the rutile structure; both are the minority component. The smallest particles throughout the SAXS represent the largest volume fraction, as do the smallest particles in the PDF analysis, which have the anatase structure.

Based on these correspondences between the TiO_2 polymorphs and physical particle size, the threshold sizes for the metastable polymorphs seen here are as follows: anatase ∼6.5 nm, brookite ∼14 nm, and rutile ∼18 nm. These thresholds are within or smaller than the previously reported ranges (anatase <11 nm, brookite 11−35 nm, and rutile >35 nm).[14,15] The increase in the volume fraction of populations of particles of discrete sizes during TiO_2 formation, without a corresponding increase in the average size of each population, suggests ongoing particle nucleation and growth up to a characteristic threshold particle size. In this scenario, the activation energy for structural transformation from one polymorph to another polymorph, that is stabilized for larger particles, must be greater than the energy required to nucleate a new particle. So, TiO_2 forms by nucleation of new particles that grow up to a threshold limit, with these particles nucleating in different chemical environments as the reaction evolves (Figure 6).

With respect to experiment design, an implication of the separation and progressive sedimentation observed here is that the abundance of the product at an arbitrary height within the solution depends on the time point in the reaction and what is both above and below. Any *in situ* experiment that uses a fine beam to probe the reaction state will yield observations that convolute the system chemistry and the specific geometry of the experiment. This complicates the interpretation and limits the general applicability of the results. Experiments using the same reaction parameters, but undertaken using different reactors or with the probe beam at different heights, may yield ostensibly different results. This includes experiments utilizing X-ray scattering and spectroscopy[38] and laser-based tools (e.g., dynamic light scattering).

Importantly, we note that this phase separation means that different trends in the species are evident as a function of height within the solution, as the product sediments. Probing the middle of the solution[39] *vs* near the surface yields a different picture of the reaction progress. Without considering the reaction heterogeneity and the settling of the product, interpretations of *in situ* experiments can both overestimate and underestimate the product yields at different points in the reaction. At intermediate heights within the solution (Supporting Information), solid sinking from the overlying solution could be misinterpreted as a sudden increase in product formation. Solid sinking from within the sample volume being probed could be misinterpreted as a sudden loss, redissolution, or transformation of the product. Within the column of solid accumulated at the bottom of the reactor, an invariance of the signal could be misinterpreted as the reaction reaching completion.

Reliable insights into the reaction evolution requires experimental design that considers the reaction heterogeneity.[40] For example, focusing the analysis just beneath the solution surface deconvolutes the kinetics from emergent spatial heterogeneity. Alternatively, experiments could raster the beam over the full reaction height or use probes that encompass the entire reaction system (e.g., neutrons).

CONCLUSIONS

By establishing time-lapse optical imaging as a probe of hydrothermal reactions, we achieve an effective, accessible, and low-cost means to screen or compare many (10s−100s) different reaction conditions simultaneously, with greater consistency. This opens the door to systematic investigations of how key reaction parameters impact kinetics, particle size, and phase segregation. While the reaction probed here is colorless, the *RGB* values used to evaluate luminosity in the color-corrected images can equally be applied to evaluate hue, quantifying color and, more importantly, how the color of a solution or product may change as the reaction evolves.

Compared to *in situ* X-ray PDF studies, the kinetic insights have greater sensitivity and higher signal-to-noise discrimination. Furthermore, reactions can be monitored for much longer continuous time periods than is practical using synchrotron X-rays. Because there is a correlation between the depth of the accumulated solid and the reaction time at which it settled during the reaction, there is the additional possibility of mapping the reaction *post facto* as a function of the product depth. This new approach provides a foundation for understanding and optimizing synthesis of TiO_2 and other materials prepared using similar conditions such as metal−organic frameworks, paving the way for more precise, uniform, and targeted materials synthesis.[41] Finally, this new approach has potential in real-time monitoring of pilot studies for scale-up materials from the research laboratory and during industrial manufacturing.

ASSOCIATED CONTENT

Supporting Information

The Supporting Information is available free of charge at https://pubs.acs.org/doi/10.1021/jacs.4c00749.

Details of TiO_2 synthesis, *in situ* SAXS and PDF measurements and analysis, *ex situ* transmission electron microscopy, time-lapse optical imaging, luminance, and particle size analyses (PDF)

Time-lapse video of synthesis reactions (MP4)

AUTHOR INFORMATION

Corresponding Author

Karena W. Chapman − *Department of Chemistry, Stony Brook University, Stony Brook, New York 11794, United States;* orcid.org/0000-0002-8725-5633; Email: karena.chapman@stonybrook.edu

Authors

Bryan A. Sanchez Monserrate − *Department of Chemistry, Stony Brook University, Stony Brook, New York 11794, United States;* orcid.org/0000-0001-9191-9968

Michelle L. Beauvais − *Department of Chemistry, Stony Brook University, Stony Brook, New York 11794, United States;* orcid.org/0000-0002-0349-0848
Simon M. Vornholt − *Department of Chemistry, Stony Brook University, Stony Brook, New York 11794, United States;* orcid.org/0000-0001-9490-3785
Peter J. Chupas − *Department of Chemistry, Stony Brook University, Stony Brook, New York 11794, United States; Department of Geosciences, Stony Brook University, Stony Brook, New York 11794, United States*
John B. Parise − *Department of Geosciences, Stony Brook University, Stony Brook, New York 11794, United States*

Complete contact information is available at: https://pubs.acs.org/10.1021/jacs.4c00749

Notes

The authors declare no competing financial interest.

■ ACKNOWLEDGMENTS

This work was supported as part of GENESIS: A Next Generation Synthesis Centre, an Energy Frontier Research Centre funded by the U.S. Department of Energy, Office of Science, Basic Energy Sciences under award number DESC0019212. B.S.M and M.L.B. received support as a part of QuADS: Quantitative Analysis of Dynamic Structures National Science Foundation Research Traineeship Program, grant number NSF DGE 1922639. This research used resources at beamline 11-ID-B of the Advanced Photon Source, a U.S. DOE Office of Science User Facility operated for the DOE Office of Science by Argonne National Laboratory under contract no. DE-AC02-06CH11357. This research used resources at beamlines 11-BM and 28-ID-1 of the National Synchrotron Light Source-II, a U.S. Department of Energy (DOE) Office of Science User Facility operated for the DOE Office of Science by Brookhaven National Laboratory under contract no. DE-SC0012704.

■ REFERENCES

(1) Darr, J. A.; Zhang, J.; Makwana, N. M.; Weng, X. Continuous Hydrothermal Synthesis of Inorganic Nanoparticles: Applications and Future Directions. *Chem. Rev.* **2017**, *117* (17), 11125−11238.
(2) Chen, Y.; Fan, Z.; Zhang, Z.; Niu, W.; Li, C.; Yang, N.; Chen, B.; Zhang, H. Two-Dimensional Metal Nanomaterials: Synthesis, Properties, and Applications. *Chem. Rev.* **2018**, *118* (13), 6409−6455.
(3) Zhao, X.; Jia, Y.; Wallace, G. Q.; Bazuin, C. G.; Masson, J.-F. Interrelated Roles of Multiple Key Structure-Directing Agents in Seed-Mediated Growth of Monodisperse and Multibranched Au Nanoparticles. *ChemPhysChem* **2023**, *24* (13), No. e202200842.
(4) Cargnello, M.; Gordon, T. R.; Murray, C. B. Solution-Phase Synthesis of Titanium Dioxide Nanoparticles and Nanocrystals. *Chem. Rev.* **2014**, *114* (19), 9319−9345.
(5) Yang, H. G.; Liu, G.; Qiao, S. Z.; Sun, C. H.; Jin, Y. G.; Smith, S. C.; Zou, J.; Cheng, H. M.; Lu, G. Q. Solvothermal Synthesis and Photoreactivity of Anatase TiO2 Nanosheets with Dominant {001} Facets. *J. Am. Chem. Soc.* **2009**, *131* (11), 4078−4083.
(6) Tachikawa, T.; Yamashita, S.; Majima, T. Evidence for Crystal-Face-Dependent TiO2 Photocatalysis from Single-Molecule Imaging and Kinetic Analysis. *J. Am. Chem. Soc.* **2011**, *133* (18), 7197−7204.
(7) Schneider, J.; Matsuoka, M.; Takeuchi, M.; Zhang, J.; Horiuchi, Y.; Anpo, M.; Bahnemann, D. W. Understanding TiO2 Photocatalysis: Mechanisms and Materials. *Chem. Rev.* **2014**, *114* (19), 9919−9986.
(8) Chen, X.; Mao, S. S. Titanium Dioxide Nanomaterials: Synthesis, Properties, Modifications, and Applications. *Chem. Rev.* **2007**, *107* (7), 2891−2959.
(9) Manley, D. W.; McBurney, R. T.; Miller, P.; Howe, R. F.; Rhydderch, S.; Walton, J. C. Unconventional Titania Photocatalysis: Direct Deployment of Carboxylic Acids in Alkylations and Annulations. *J. Am. Chem. Soc.* **2012**, *134* (33), 13580−13583.
(10) Ichijo, T.; Sato, S.; Fujita, M. Size-Mass-and Density-Controlled Preparation of TiO2 Nanoparticles in a Spherical Coordination Template. *J. Am. Chem. Soc.* **2013**, *135* (18), 6786−6789.
(11) Naldoni, A.; Altomare, M.; Zoppellaro, G.; Liu, N.; Kment, S.; Zbořil, R.; Schmuki, P. Photocatalysis with Reduced TiO2: From Black TiO2 to Cocatalyst-Free Hydrogen Production. *ACS Catal.* **2019**, *9* (1), 345−364.
(12) Nonoyama, T.; Kinoshita, T.; Higuchi, M.; Nagata, K.; Tanaka, M.; Sato, K.; Kato, K. TiO2 Synthesis Inspired by Biomineralization: Control of Morphology, Crystal Phase, and Light-Use Efficiency in a Single Process. *J. Am. Chem. Soc.* **2012**, *134* (21), 8841−8847.
(13) Símonarson, G.; Sommer, S.; Lotsari, A.; Elgh, B.; Iversen, B. B.; Palmqvist, A. E. C. Evolution of the Polymorph Selectivity of Titania Formation under Acidic and Low-Temperature Conditions. *ACS Omega* **2019**, *4* (3), 5750−5757.
(14) Finnegan, M. P.; Zhang, H.; Banfield, J. F. Phase Stability and Transformation in Titania Nanoparticles in Aqueous Solutions Dominated by Surface Energy. *J. Phys. Chem. C* **2007**, *111* (5), 1962−1968.
(15) Ranade, M. R.; Navrotsky, A.; Zhang, H. Z.; Banfield, J. F.; Elder, S. H.; Zaban, A.; Borse, P. H.; Kulkarni, S. K.; Doran, G. S.; Whitfield, H. J. Energetics of nanocrystalline TiO2. *Proc. Natl. Acad. Sci. U.S.A.* **2002**, *99* (suppl_2), 6476−6481.
(16) Zhang, H.; Banfield, J. F. Understanding Polymorphic Phase Transformation Behavior during Growth of Nanocrystalline Aggregates: Insights from TiO2. *J. Phys. Chem. B* **2000**, *104* (15), 3481−3487.
(17) He, Y. T.; Wan, J.; Tokunaga, T. Kinetic stability of hematite nanoparticles: the effect of particle sizes. *J. Nanopart. Res.* **2008**, *10* (2), 321−332.
(18) Navrotsky, A. Energetics of nanoparticle oxides: interplay between surface energy and polymorphism†. *Geochem. Trans.* **2003**, *4* (1), 34.
(19) Phan, H. T.; Haes, A. J. What Does Nanoparticle Stability Mean? *J. Phys. Chem. C* **2019**, *123* (27), 16495−16507.
(20) Strach, M.; Mantella, V.; Pankhurst, J. R.; Iyengar, P.; Loiudice, A.; Das, S.; Corminboeuf, C.; van Beek, W.; Buonsanti, R. Insights into Reaction Intermediates to Predict Synthetic Pathways for Shape-Controlled Metal Nanocrystals. *J. Am. Chem. Soc.* **2019**, *141* (41), 16312−16322.
(21) Zhang, Z.; Wu, Q.; Johnson, G.; Ye, Y.; Li, X.; Li, N.; Cui, M.; Lee, J. D.; Liu, C.; Zhao, S.; et al. Generalized Synthetic Strategy for Transition-Metal-Doped Brookite-Phase TiO2 Nanorods. *J. Am. Chem. Soc.* **2019**, *141* (42), 16548−16552.
(22) Sun, Y.; Ren, Y. In Situ Synchrotron X-Ray Techniques for Real-Time Probing of Colloidal Nanoparticle Synthesis. *Part. Part. Syst. Charact.* **2013**, *30* (5), 399−419.
(23) Chupas, P. J.; Chapman, K. W.; Jennings, G.; Lee, P. L.; Grey, C. P. Watching Nanoparticles Grow: The Mechanism and Kinetics for the Formation of TiO2-Supported Platinum Nanoparticles. *J. Am. Chem. Soc.* **2007**, *129* (45), 13822−13824.
(24) Jensen, K. M. Ø.; Christensen, M.; Juhas, P.; Tyrsted, C.; Bøjesen, E. D.; Lock, N.; Billinge, S. J. L.; Iversen, B. B. Revealing the Mechanisms behind SnO2 Nanoparticle Formation and Growth during Hydrothermal Synthesis: An In Situ Total Scattering Study. *J. Am. Chem. Soc.* **2012**, *134* (15), 6785−6792.
(25) Skjærvø, S. L.; Wells, K. H.; Sommer, S.; Vu, T.-D.; Tolchard, J. R.; van Beek, W.; Grande, T.; Iversen, B. B.; Einarsrud, M.-A. Rationalization of Hydrothermal Synthesis of NaNbO3 by Rapid in Situ Time-Resolved Synchrotron X-ray Diffraction. *Cryst. Growth Des.* **2018**, *18* (2), 770−774.
(26) Skjærvø, S. L.; Wells, K. H.; van Beek, W.; Grande, T.; Einarsrud, M.-A. Kinetics during hydrothermal synthesis of nanosized KxNa1-xNbO3. *CrystEngComm* **2018**, *20* (42), 6795−6802.

(27) Petkov, V.; Cozzoli, P. D.; Buonsanti, R.; Cingolani, R.; Ren, Y. Size, Shape, and Internal Atomic Ordering of Nanocrystals by Atomic Pair Distribution Functions: A Comparative Study of γ-Fe2O3 Nanosized Spheres and Tetrapods. *J. Am. Chem. Soc.* **2009**, *131* (40), 14264−14266.
(28) Sanchez Monserrate, B. A.; Grenier, A.; Chupas, P. J.; Chapman, K. W. A high-temperature sample changer for parallelized in situ X-ray studies to efficiently explore reaction space. *J. Appl. Crystallogr.* **2023**, *56* (6), 1732−1738.
(29) Massingberd-Mundy, F.; Poulston, S.; Bennett, S.; Yeung, H. H.-M.; Johnson, T. Use of open source monitoring hardware to improve the production of MOFs: using STA-16(Ni) as a case study. *Sci. Rep.* **2020**, *10* (1), 17355.
(30) Khlebtsov, B. N.; Khanadeev, V. A.; Khlebtsov, N. G. Determination of the Size, Concentration, and Refractive Index of Silica Nanoparticles from Turbidity Spectra. *Langmuir* **2008**, *24* (16), 8964−8970.
(31) Zhao, J.; Tian, S.; Xie, H.; Zhang, X. Study of Time-Varying Laws of Stability and Wettability of SiO2-H2O Nanofluids with Different Particle Sizes. *Ind. Eng. Chem. Res.* **2023**, *62* (34), 13529−13540.
(32) Farrow, C. L.; Juhas, P.; Liu, J. W.; Bryndin, D.; Božin, E. S.; Bloch, J.; Proffen, T.; Billinge, S. J. L. PDFfit2 and PDFgui: computer programs for studying nanostructure in crystals. *J. Phys.: Condens. Matter* **2007**, *19* (33), 335219.
(33) Buonsanti, R.; Carlino, E.; Giannini, C.; Altamura, D.; De Marco, L.; Giannuzzi, R.; Manca, M.; Gigli, G.; Cozzoli, P. D. Hyperbranched Anatase TiO2 Nanocrystals: Nonaqueous Synthesis, Growth Mechanism, and Exploitation in Dye-Sensitized Solar Cells. *J. Am. Chem. Soc.* **2011**, *133* (47), 19216−19239.
(34) Dalod, A. R. M.; Grendal, O. G.; Skjærvø, S. L.; Inzani, K.; Selbach, S. M.; Henriksen, L.; van Beek, W.; Grande, T.; Einarsrud, M.-A. Controlling Oriented Attachment and in Situ Functionalization of TiO2 Nanoparticles During Hydrothermal Synthesis with APTES. *J. Phys. Chem. C* **2017**, *121* (21), 11897−11906.
(35) Zhang, X.; Tran, S.; Gray-Weale, A. Hydrodynamic Drag on Diffusing Nanoparticles for Size Determination. *J. Phys. Chem. C* **2016**, *120* (38), 21888−21896.
(36) Li, Z. Critical particle size where the Stokes-Einstein relation breaks down. *Phys. Rev. E* **2009**, *80* (6), 061204.
(37) Schmidt, J. R.; Skinner, J. L. Hydrodynamic boundary conditions, the Stokes-Einstein law, and long-time tails in the Brownian limit. *J. Chem. Phys.* **2003**, *119* (15), 8062−8068.
(38) Koziej, D. Revealing Complexity of Nanoparticle Synthesis in Solution by in Situ Hard X-ray Spectroscopy—Today and Beyond. *Chem. Mater.* **2016**, *28* (8), 2478−2490.
(39) Grunwaldt, J.-D.; Ramin, M.; Rohr, M.; Michailovski, A.; Patzke, G. R.; Baiker, A. High pressure in situ x-ray absorption spectroscopy cell for studying simultaneously the liquid phase and the solid/liquid interface. *Rev. Sci. Instrum.* **2005**, *76* (5), 054104.
(40) Jeppesen, H. S.; Nielsen, I. G.; Kondrup, J. C.; Just, J.; Lock, N. LiquidReactionCell - a versatile setup for in situ synchrotron studies of compounds in liquid suspension and solution. *CrystEngComm* **2023**, *25* (5), 751−760.
(41) Liu, Y.; Yang, Y.; Sun, Y.; Song, J.; Rudawski, N. G.; Chen, X.; Tan, W. Ostwald Ripening-Mediated Grafting of Metal-Organic Frameworks on a Single Colloidal Nanocrystal to Form Uniform and Controllable MXF. *J. Am. Chem. Soc.* **2019**, *141* (18), 7407−7413.

https://doi.org/10.1021/jacs.4c00749
J. Am. Chem. Soc. 2024, 146, 10745−10752